ARTICLE

Effects of Incorporating Steel Fibers and Municipal Waste on the Compressive Strength of Concrete

Xiangmiao Wan, Yan Tan[*] and Xiong Long

School of Civil Architecture and Environment, Hubei University of Technology, Wuhan, 430068, China

[*]Corresponding Author: Yan Tan. Email: tanyan@hbut.edu.cn

Received: 04 January 2024　　Accepted: 15 March 2024

ABSTRACT

In this study, we assessed the impact of substituting natural fine aggregates with municipal solid waste incineration bottom ash (MSWI-BA) in steel fiber (SF)-reinforced concrete on its compressive properties post high-temperature exposure. The concrete specimens incorporating MSWI-BA as the fine aggregate and SFs for reinforcement underwent uniaxial compression tests after exposure to high temperatures. Through the tests, we investigated the impact of high-temperature exposure on mechanical properties, such as mass loss rate, stress-strain full curve, compressive strength, peak strain, elastic modulus, and so on, over different thermostatic durations. The analysis revealed that with the increasing exposure temperature and durations, the mass loss rate gradually increased; compressive strength initially increased and then decreased; peak strain significantly increased; stress-strain curve flattened, and elasticity modulus monotonically decreased. Different thermostatic durations led to distinct critical temperatures for the compressive strength (700°C for 1.0 and 1.5 h, and 500°C for 2 h). The concrete specimens exhibited an increasing compressive strength below the critical temperature, followed by a rapid decrease upon exceeding it. Based on the strain equivalence hypothesis and Weibull distribution theory, we derived expressions for the total damage variables and a uniaxial compression constitutive model, which accurately reflected the changing macro mechanical properties of concrete under various exposure temperatures and thermostatic durations. The concrete matrix microscopic morphology continuously deteriorated beyond 500°C, resulting in a loss of compressive strength. This degradation in the concrete microstructure serves as the fundamental cause for the decline in its macroscopic mechanical properties.

KEYWORDS

Municipal solid waste incineration bottom ash; steel fiber; high temperature; uniaxial compression; damage pattern

1 Introduction

　　Waste management is a pressing global environmental concern, with daily municipal solid waste generated requiring effective control [1,2]. Currently, two primary methods, namely sanitary landfilling and incineration, are employed to address these issues [3–5]. In the incineration process, the main solid products are fly ash and bottom residue (municipal solid waste incineration bottom ash; MSWI-BA) [6–8]. MSWI-BA can substitute certain fine natural aggregates in concrete, owing to similar physical properties. This can minimize (i) domesticwaste disposal pressures, (ii) MSWI-BA landfilling issues, and (iii) environmental pollution [9–11]. It further reduces the demand for sand and gravel extraction [12].

This practice is consistent with the ideas of sustainable development and helps promote resource recycling and environmental protection [13–15].

Studies on the use of MSWI-BA as a substitute for natural aggregates have gained significant interest in recent years. Concrete mixed with MSWI-BA shows a slight decrease in mechanical properties compared to traditional concrete, but meets usage requirements [16,17]. Moreover, the addition of MSWI-BA enhances concrete durability by reducing coarse capillary porosity [6]. Li et al. [14] found that the chloride permeability of eco-SCM deteriorates by adding MSWI-BA, however, with insufficient durability. Thomas et al. [18] revealed that upon inducing freeze-thaw cycles, the frost and abrasion resistance of mortars made with MSWI slag were comparable to or even higher than those made with natural aggregates. To summarize, MSWI-BA-reinforced concrete meets engineering requirements for durability, mechanical properties, and workability, offering advantages, such as reduced production costs, carbon footprint, and energy consumption compared to ordinary concrete [13].

The resistance of concrete to extreme environmental conditions is a crucial aspect of durability analysis. With the increasing complexity of engineering structures, it is crucial to study the mechanical properties of concrete under events of fires and explosions [19–23]. Studies on MSWI-BA mixtures have indicated that its incorporation can reduce the thermal conductivity of the concrete mix [24]. However, excessive amounts (>6%) may lead to matrix cracking due to low activity and porosity, potentially affecting high-temperature performance [25].

Fibers can be incorporated within concrete to improve its refractory properties [26–28]. Steel fibers (SFs) can significantly enhance the mechanical properties of concrete after exposure to high temperatures [29–32]. Specifically, SF reinforcement in concrete has been shown to (i) improve residual shear strength compared that of ordinary concrete [33]; (ii) prevent spalling and significantly improve the ductility and cracking behavior after exposure to high temperatures [34]; and (iii) effectively increase the high-temperature residual strength and improve the damage mode, while enhancing the toughness and fracture energy [35]. Yang et al. [36] found that an appropriate BF volume content can reduce the damage degree and failure mode of BFRC. However, the high-temperature performance of fiber-reinforced concrete still requires systematic analysis to better understand the underlying mechanisms behind the performance changes. Shen et al. [37,38] proposed a four-step multi-scale homogenization method to predict the SFRC thermal conductivity evolution at high temperatures, while considering the effect of crack resistance (cracks can occur due to high temperatures, water loss, and dehydration). Yu et al. [39] established a constitutive model based on the Drucker Prager model [40], considering the coupled effect of high temperature and high strain rate on concrete. In the abovementioned studies, experimental data was used to establish simplified relationships, expressing thermal conductivity or strain rate as a function of temperature to quantitatively determine its impact on concrete. Singh et al. [41] explored the use of MSWI-BA in fiber-reinforced concrete and its impact on the mechanical properties.

In this study, we aimed to further investigate the effects of adding MSWI-BA in concrete, especially post SF reinforcement. We constructed concrete specimens using MSWI-BA and SFs, and performed uniaxial compression tests after exposing the specimens to high temperatures. The effect of varied heating temperatures and thermostatic durations on the compressive strength, peak strain, and elastic modulus of the specimens were analyzed. Additionally, microstructural changes in the specimens were observed via scanning electron microscopy (SEM), revealing the strength degradation from both macroscopic and microscopic perspectives. Using the experimental results, a constitutive model and total damage evolution equation were established based on the strain equivalence principle to evaluate the damage evolution in thermally damaged MSWI-BA-and SF-SF-reinforced concrete. This study can promote the widespread application of MSWI-BA-and SF-reinforced concrete in engineering practice and the development of new green concrete fields.

2 Experimental Design

2.1 Materials

The cementitious materials employed in this study include ordinary silicate cement (PO 42.5) and class I fly ash. Well-graded river sand with a fineness modulus of 2.61 was used as the fine aggregate, while the coarse aggregate consisted of crushed stone with a particle size in the range of 5–20 mm. Additionally, a polycarboxylic-acid-based high-efficiency water-reducing agent was incorporated to effectively lower the water-cement ratio and enhance the compressive strength. Standard tap water, meeting national quality standards, was used for mixing. To enhance the refractoriness of the concrete, copper-plated SFs were selected for reinforcement (Fig. 1; Table 1). These fibers boast of high tensile strength and modulus of elasticity, improving toughness, crack resistance, and fatigue resistance in concrete. Moreover, they mitigate concrete spalling during exposure to high temperatures. The activated filler, MSWI-BA, was sourced from the raw bottom ash of a waste incineration power plant in Wuhan, China. Post-processing yielded fine particles with a maximum particle size of 5 mm (Fig. 2; Table 2).

Figure 1: MSWI-BA fine aggregates

Table 1: Copper-plated SF performance indicators

Length/mm	Diameter/mm	Tensile strength/MPa	Density/(g·m^{-3})
13	0.18~0.23	≥3000	7.80

2.2 Mixing Ratios

We explored various aspects of SF-reinforced concrete [42–44]. Based on the optimal SF volume admixture range of 0.5%–1.5% for reinforcing concrete [45,46], we fixed the SF volume to 1.0% for our test specimens. Preliminary tests were conducted to determine the optimum MSWI-BA content in concrete and its impact on the compressive and flexural strength of the specimens over a range of temperatures (Table 3).

Figure 2: Copper-plated SFs

Table 2: MSWI-BA physical properties

Bulk density/(kg/m^3)	Apparent density/(kg/m^3)	Water absorption/%	Void rate/%	Crushing index/%
1192	2430	10.5	41.2	31.1

Table 3: Concrete mixing ratios (kg/m^3)

MSWI-BA dosage	Water	Cement	Sand	MSWI-BA	Gravel	Fly ash	Steel fiber
0	195.0	436.0	558.0	0	1134.0	77.0	78.0
20	195.0	436.0	446.4	111.6	1134.0	77.0	78.0
40	195.0	436.0	334.8	223.2	1134.0	77.0	78.0

2.3 Specimen Preparation

To address the high water absorption of MSWI-BA, a pre-wetting process was implemented to ensure water-cement ratio uniformity in the concrete specimens. The pre-wetting mixing procedure involved soaking the MSWI-BA aggregates in water for 3 min. Subsequently, sand, MSWI-BA aggregate, gravel, cement, and fly ash were weighed and poured into the vibrating mixer for dry mixing for 1 min. Subsequently, the net water consumption was added gradually over a 2-min mixing process, incorporating SFs. Each group produced three specimen cubes of dimensions 100 mm × 100 mm × 100 mm. These specimens were demolded after 24 h and placed in a curing room at (20 ± 2)°C with over 95% humidity for 28 d before conducting the high-temperature tests.
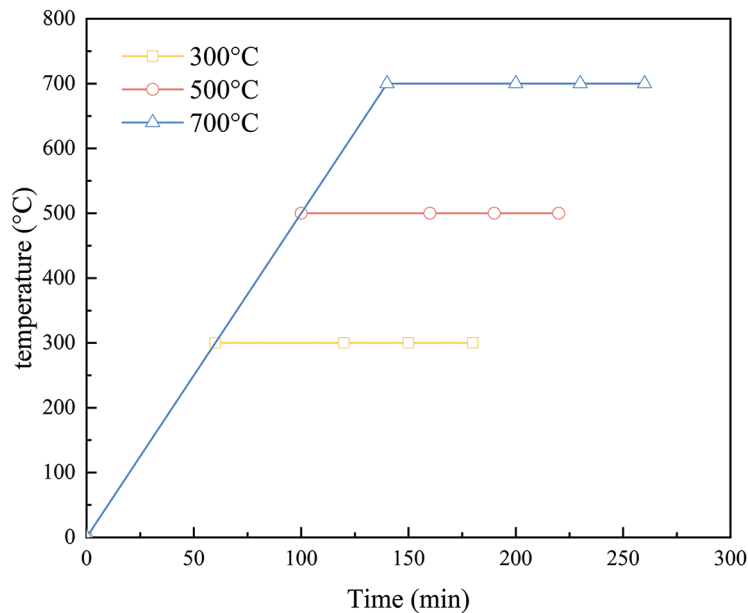
2.4 Thermal Exposure Test

After completing the curing process, the specimens were placed in a 60°C oven for 1 d to facilitate drying and removal of excess water. Subsequently, high-temperature tests were performed using

a SX2-4-10N box resistance furnace, which has a maximum heating temperature of 800°C and a maximum heating rate of 30°C/min. Currently, there exists no standard protocol for subjecting concrete specimens to high temperatures. The following protocols have been employed in previous studies: Varona et al. [47] used heating rates of 4.6–8.3°C/min and a dwell time of 75 min for cylindrical specimens with a diameter of 76.4 mm; Zhang et al. [48] used heating rates of 5–12.0°C/min and a dwell time of 180 min for cubic specimens with a side length of 150.0 mm; and Li et al. [49] used a heating rate of 3.3°C/min and a dwell time of 2 h for cylindrical specimens with a diameter of 140.0 mm. To achieve all target temperatures within a reasonable timeframe while preventing specimen cracking due to excessive heat, we set the heating rate to 5°C/min. We primarily focused on the effect of high-temperature exposure time on the degree of concrete damage. Therefore, upon reaching the target temperature, we maintained the temperature for 1.0, 1.5, and 2.0 h. Subsequently, the furnace was switched off and the samples were naturally cooled to room temperature within the furnace (the cooling rate was not controlled). The specimens were tested within 24 h after the heating and cooling process. All specimens were weighed using an electronic weighing scale with a range of 0–20 kg and an accuracy of 0.1 g before and after heating to determine weight loss due to thermal exposure (Table 4; Fig. 3).

Table 4: Concrete specimen experimental test designs and compressive strength

Number	T/°C	H/h	f_T/GPa	Number	T/°C	H/h	f_T/GPa
T25	25	0	48.1	T500-H1.5	500	1.5	48.9
T300-H1	300	1	51.8	T500-H2	500	2	43.2
T300-H1.5	300	1.5	56.6	T700-H1	700	1	42.3
T300-H2	300	2	61.4	T700-H1.5	700	1.5	35.5
T500-H1	500	1	53.2	T700-H2	700	2	29.4

Figure 3: Concrete specimen heating process

2.5 Mechanical Performance Test

The compressive strength tests were conducted on a universal testing machine with a loading rate of 0.5 MPa/s (Fig. 4). To measure the axial strain during compression, strain gauges (length = 50 mm) were affixed axially onto the cubic specimen surface. A high-speed static data acquisition instrument was used to collect strain data, and the acquired force and deformation data were utilized to construct the stress-strain curves.

Figure 4: Compressive strength test setup

Here, f_T represents the cube compressive strength of the concrete specimens after high-temperature exposure; T is the heating temperature; and H is the thermostatic duration.

3 Results and Analysis
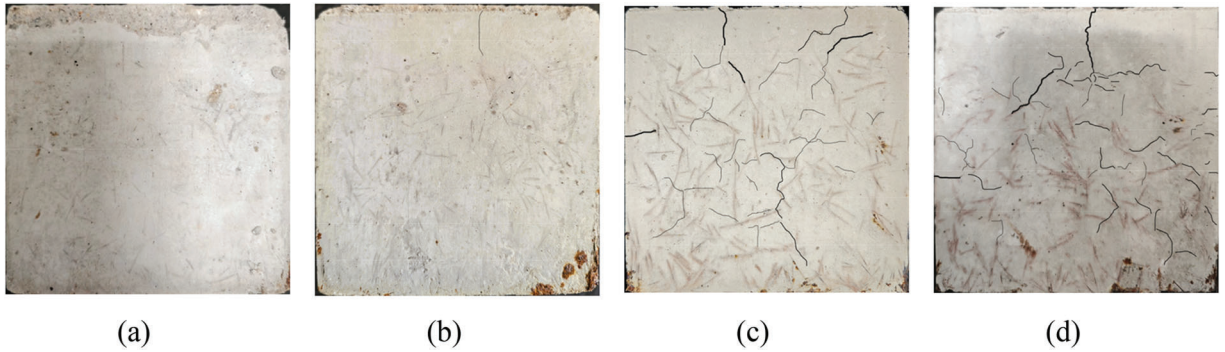
3.1 Multiscale Analysis

3.1.1 Surface Morphology

We analyzed the evolving appearance of the concrete specimens exposed to various temperatures (Fig. 5). Initially, at ambient temperature, the specimens exhibited rough and uneven surfaces, characterized by a brittle and friable texture, with numerous unevenly distributed surface pores. This can be attributed to the reaction between metallic aluminum (Al) in IBA and concrete, leading to the generation and escape of hydrogen (H), which results in the expansion and cracking of the hardened cement paste. Upon exposure to elevated temperatures, the color of the specimens gradually darkened and surface pores and cracks became more pronounced. Although at 300°C, the surfaces displayed no evident cracks, at 500°C, the cracking significantly increased, accompanied by brownish-red traces of oxidized SFs. Further, at 700°C, the brownish-red traces intensified and crack width increased with the intersection of smaller cracks. These observations highlighted 500°C as a critical temperature threshold for surface damage in the concrete specimens. Beyond this point, increasing the temperature noticeably enhanced surface damage.
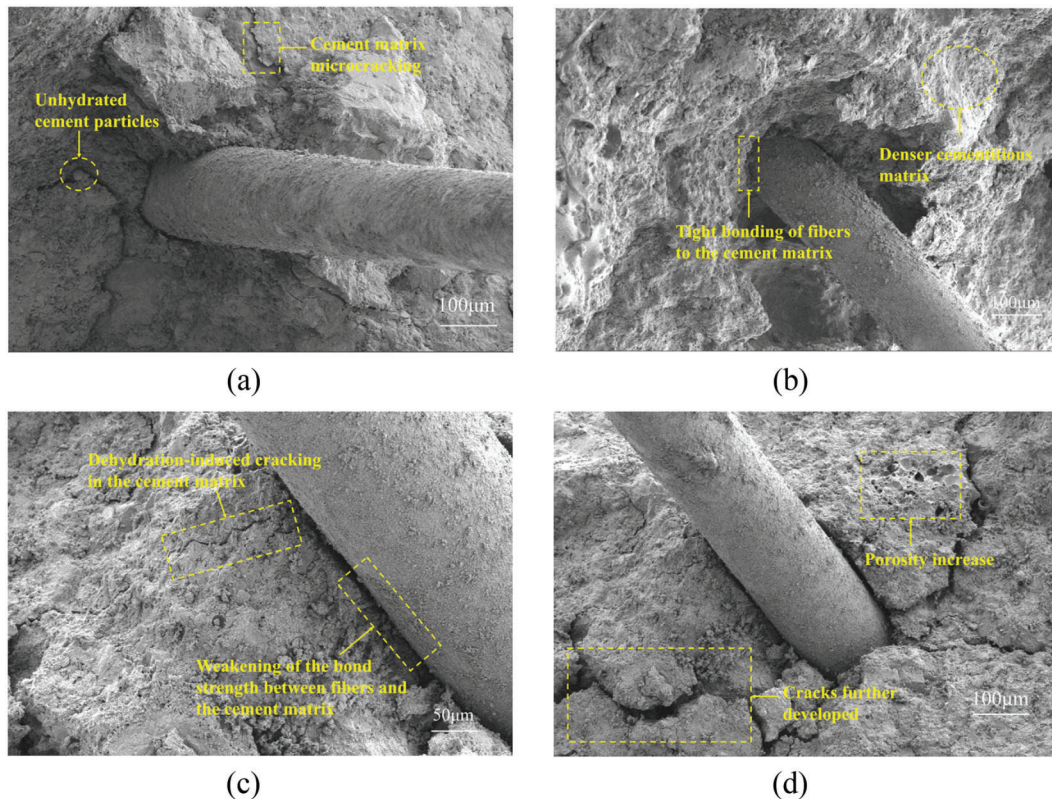
3.1.2 Microscopic Analysis

The SEM images of the specimens at room temperature revealed the cement matrix to be flat and dense, with SFs uniformly covered by hydration products, forming a strong bond (Fig. 6a). Some residual cement particles were observed on the matrix surface due to the high porosity of MSWI-BA. These particles were drawn into the pores with water, hindering complete participation in the hydration reaction. Additionally,

matrix holes and microcracks occurred due to Al-induced H generation in MSWI-BA. At 300°C, the specimens exhibited a high-temperature strengthening effect, with secondary hydration of cement particles generating additional C–S–H gels and forming a denser matrix structure. This resulted in a macroscopic increase in the concrete strength compared to ambient conditions (Fig. 6b). At 500°C, distinct cracks emerged in the cement matrix, impacting its densification (Fig. 6c). Concurrently, a decrease in the hydration products on the SF surfaces weakened their adhesion to the matrix, resulting in a lower macroscopic strength compared to that at 300°C. Upon exposure to 700°C, the cement matrix displayed significant looseness, characterized by numerous cracks and pores, and experienced a notable reduction in C–S–H gel content (Fig. 6d). These factors collectively contributed to a sharp decrease in the specimen strength.

(a)   (b)   (c)   (d)

Figure 5: Surface morphological changes in the concrete specimens over 1.5 h of high-temperature exposure: (a) 25°C, (b) 300°C, (c) 500°C, and (d) 700°C

Figure 6: SEM images of concrete specimens after 1.5 h of high-temperature exposure: (a) 25°C, (b) 300°C, (c) 500°C, and (d) 700°C
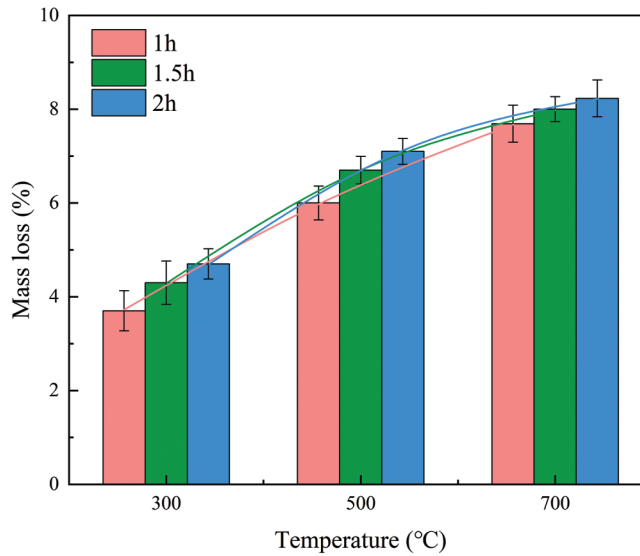
3.2 Mass Loss

The concrete specimen mass loss rate, m, after high-temperature exposure can be expressed as

$$m = \frac{m_0 - m_1}{m_0} \times 100\%, \tag{1}$$

where m_0 and m_1 are the specimen masses (kg) at room temperature and after high-temperature exposure, respectively.

The mass loss rate showed an ascending trend corresponding to higher temperatures (Fig. 7). It primarily resulted from cement matrix moisture evaporation, C–S–H gel dehydration, and cement paste cracking and peeling. Furthermore, the gradual increase in mass loss with prolonged exposure can be attributed to the low thermal conductivity of concrete, leading to non-uniform heating from the outer to inner layers at elevated temperatures. With increasing thermostatic durations at high temperatures, internal hydration products in the specimens fully decompose, further accelerating the mass loss rate.

Figure 7: Mass loss rate of concrete specimens after high-temperature exposure

3.3 Analysis of Mechanical Test Results
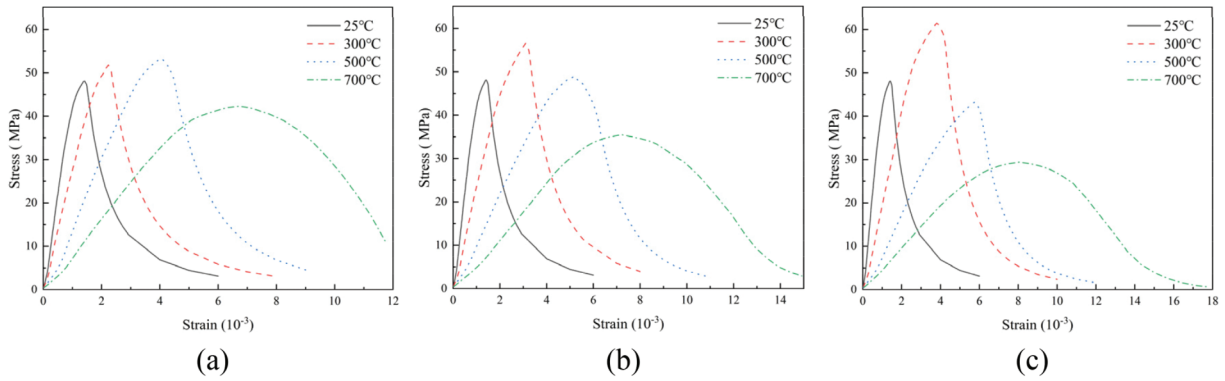
3.3.1 Stress-Strain Relationship

The uniaxial compressive stress-strain curves for the concrete specimens after different thermostatic durations were roughly divided into four stages (Fig. 8): compaction, elastic, yield, and destruction. Each of these stages is discussed below in detail:

- Compaction: The curve in this stage exhibited gradual growth. The significance of the compaction-density stage increased with the increasing temperature (Fig. 8). This can be attributed to the occurrence of pores within the initially compacted concrete specimens after high-temperature exposure due to the gradual loosening of the internal structure.
- Elastic: The curve exhibited a linear rise in this phase with an evident critical slope value (Fig. 8). Below 500°C, temperatures on the higher end promoted a secondary hydration reaction inside the specimens, repairing defects in the cement matrix, which results in a curve slope similar to that at room temperature. However, exposure to temperatures exceeding 500°C induced the decomposition of cementitious materials, gradually expanding the internal cracks in the specimens,

which manifested as a curve slope decrease. Comparing Figs. 8a–8c revealed that the curve slope for a fixed temperature decreased with prolonged exposure. This can be attributed to the increased severity of internal damage in the concrete specimens with longer exposures to a constant high temperature.

- Yield: The curve slope gradually decreased, eventually reaching peak stress. High temperatures resulted in increased internal pores and cracks in the specimens, generating internal tensile stresses and reducing adhesion between the aggregates and cement matrix. During this phase, SFs play a crucial role in bridging the aggregates and limiting crack development, enhancing the specimen ductility.

Figure 8: Stress-strain curves for concrete specimens maintained at 25°C, 300°C, 500°C, and 700°C for (a) 1.0, (b) 1.5, and (c) 2.0 h
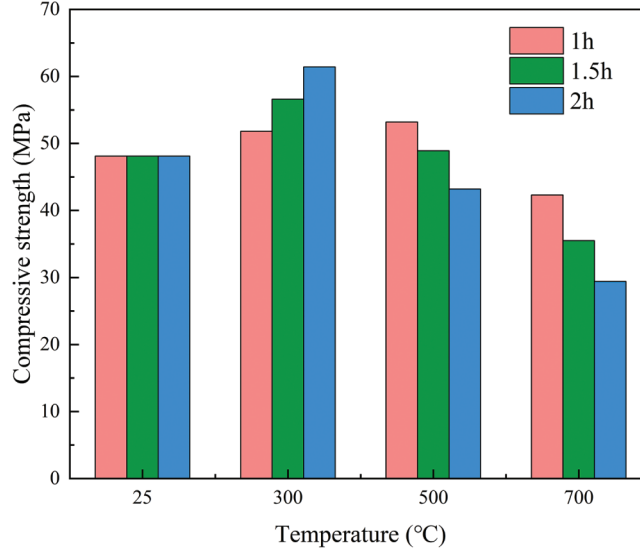
Destruction: The curve experienced an abrupt drop and the concrete specimens rapidly deteriorated. Below 500°C, concrete specimen dehydration resulted in brittleness, and the strain corresponding to the peak stress was minimal. However, above 500°C, the heat loosened the internal structure, significantly increasing the strain corresponding to the peak stress and slowing the curve declining rate.

3.3.2 Compressive Strength

The stress-strain curves of the concrete specimens after high-temperature exposure featured a peak, where the vertical coordinate corresponds to the cubic compressive strength, f_T, of the concrete specimens.

Compared to previous studies [50,51], exposing the specimens to a temperature of 300°C evaporated the free water inside the concrete specimens (Fig. 9). This process increased the contact area of the cement matrix, promoted specimen hydration, and enhanced S–C–H gel generation, resulting in a denser internal structure. Notably, the MSWI-BA aggregates did not reach the expansion temperature, contributing to the increase in the compressive strength of the concrete specimens with prolonged thermostatic durations at high temperatures. The impact of maintaining the specimens at fixed high temperatures becomes multifaceted. The internal water evaporation in the specimens promotes the formation of its internal structure, further tightening the cement paste body and connecting it securely to the SFs, thereby enhancing the overall specimen strength. On the other hand, the lack of coordination of the thermal expansion coefficients of the MSWI-BA aggregate and cement paste generates internal tensile stresses, resulting in crack formation at their interface. The interplay of these two factors results in a diametrically opposite change in compressive strength with increasing thermostatic time. For thermostatic exposure times of 1.0 and 1.5 h at 500°C, the strengthening effect of heat on concrete specimens outweighed the deterioration effect, manifesting as a slight increase in the compressive strength compared to that at 300°C. As the thermostatic duration was further increased, the strengthening effect, and hence, the compressive strength decreased after 2 h at a constant temperature. At 700°C, the matrix and C–S–H gel

attached to the SFs decomposed significantly, reducing its role in bridging the aggregate and inhibiting crack development. The expansion and deformation of the MSWI-BA aggregate further contributed to cracking within the concrete. Therefore, such high temperatures have a more deteriorative impact, resulting in a sharp decrease in specimen strength.

Figure 9: Effect of high-temperature exposure on concrete specimen compressive strength

The concrete specimens exhibited a critical temperature for compressive strength for different thermostatic durations. The critical temperature after 1.0 and 1.5 h was 700°C, and after 2 h was 500°C. Below (above) the critical temperature, the compressive strength increased (rapidly declined). Based on the experimental data, the relationship between compressive strength, exposure temperature, and thermostatic durations was fitted to obtain a correlation coefficient of 0.9629 for the following equation:

$$f_T = 46.34 + 0.057T + 4.21H - 3.5 \times 10^{-5}T^2 + 5.34H^2 - 0.05TH, \tag{2}$$
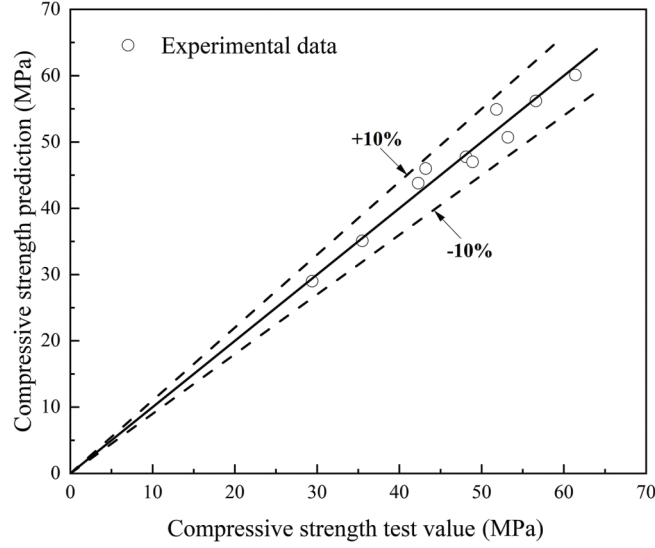
where T is the exposure temperature (°C) and H is the thermostatic duration.

Using Eq. (2), the comparison of the predicted and actual compressive strength values revealed an error rate within 10%, with a mean ratio of 1.0014 and variance of 0.0312 (Fig. 10). This indicated the effectiveness of the fitted function in predicting the compressive strength of the concrete specimens after high-temperature exposure.
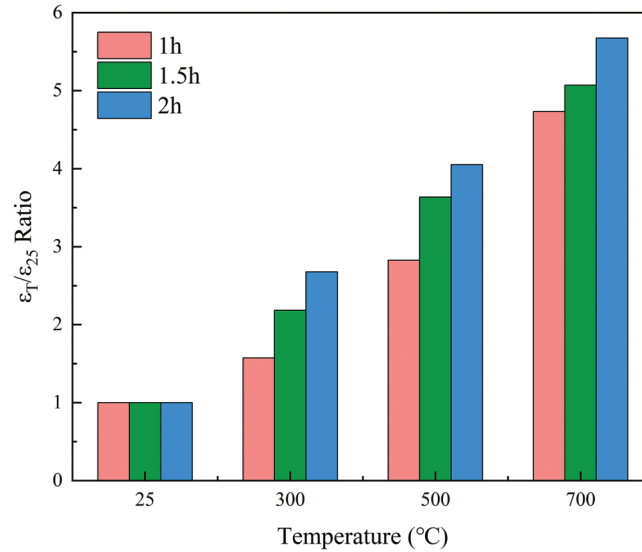
3.3.3 Peak Strain

The stress-strain curves of the concrete specimens after high-temperature exposure featured a peak strain (ε_T). To better grasp the impact of exposure temperatures and thermostatic durations, we calculated the ratio of the peak strain after high-temperature exposure (ε_T) to that at room temperature (ε_{25}), considering the latter as a benchmark. The general trend depicted an increase in this ratio with the rising exposure temperature and thermostatic duration (Fig. 11). High temperatures below 500°C induced gradual pore water evaporation and increased pressure within the concrete specimens, resulting in microcrack formation. Simultaneously, the water vapors enhanced contact with unhydrated materials in the concrete, triggering secondary hydration and generating gels that filled the pores. This consequently increased the strain within the concrete specimens gradually. However, above 500°C, the peak strain experienced a rapid increase. The SEM results (Fig. 6) combined with analysis, suggested that higher temperatures led to the (i) gradual

decomposition of the cementitious materials, and (ii) mismatch in thermal expansion coefficients of the MSWI-BA aggregate and cement paste, exacerbating crack damage in the specimens. Particularly at 700°C, significant decomposition of the cementitious material attached to SFs reduced the mechanical bonding force between them, causing cement paste spalling on the SF surface and further increasing the peak strain.

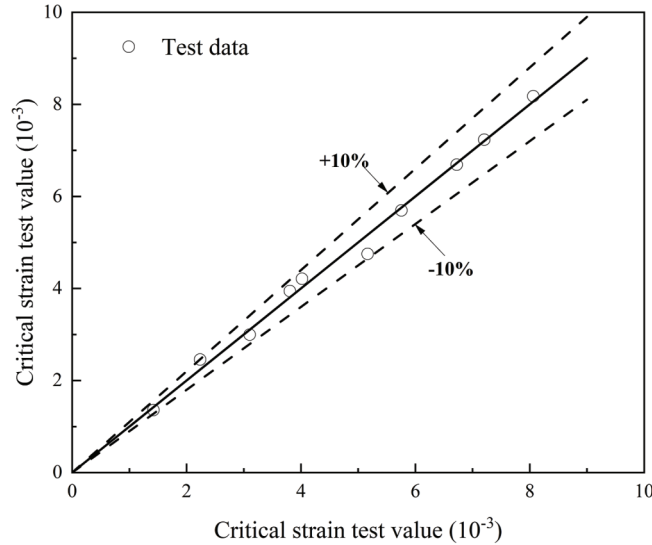**Figure 10:** Comparison of predicted and tested values of compressive strength of concrete specimens

Figure 11: Effect of high-temperature exposure on concrete specimen peak strain

The relationship between peak strain, exposure temperature, and thermostatic duration was obtained by fitting the prediction to the experimental data. We obtained a correlation coefficient of 0.9929 for the following equation:

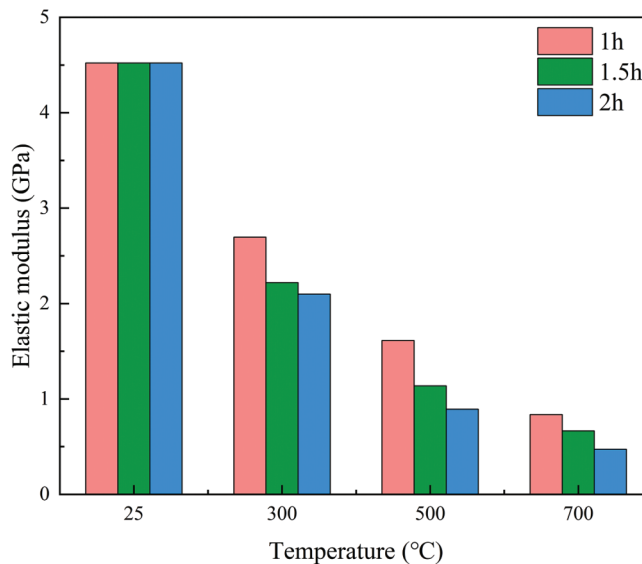$$\varepsilon_T / \varepsilon_{25} = 1.32 + 0.0015T - 0.93H + 9.09 \times 10^{-6} T^2 + 0.81 H^2. \tag{3}$$

The peak strain predictions obtained using Eq. (3) were compared with the test values (Fig. 12); the error rate was found to be within 10%, with a mean ratio value of 1.0027 and a variance of 0.0374. This indicated that the fitted function could effectively predict the peak strain of the concrete specimens after high-temperature exposure.

Figure 12: Comparison of predicted and tested values of peak strain

3.3.4 Elasticity Modulus

The elastic modulus, V_ε, of the concrete specimens decreased consistently with the rising exposure temperature (Fig. 13). Compared to the room temperature state, the concrete specimens exposed to 300°C, 500°C, and 700°C for thermostatic durations of 1.0, 1.5, and 2.0 h experienced reductions in elastic modulus by 40.39%, 64.34%, and 81.53%, 50.92%, 74.85%, and 85.29%, 53.59%, 80.27%, and 89.56%, respectively. These results underscored the substantial impact of high-temperature exposure on the elastic modulus of the concrete specimens, with higher temperatures and prolonged exposure durations resulting in a diminished ability of concrete to resist deformation.
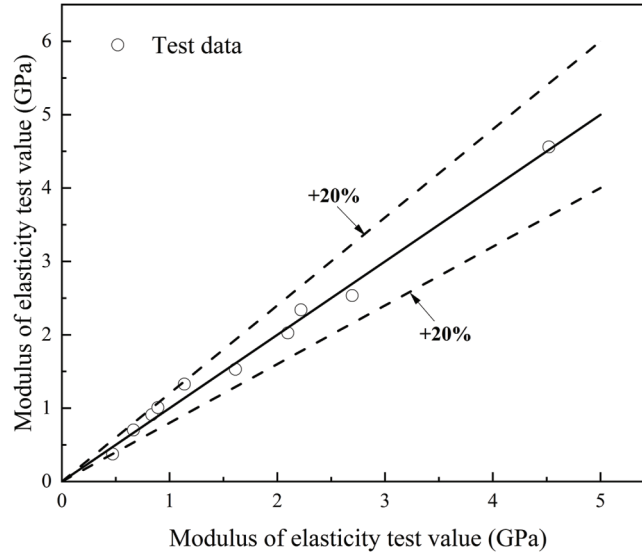

Figure 13: Elasticity modulus of concrete specimens after high-temperature exposure

We then established the relationship between the elasticity modulus, exposure temperature, and thermostatic durations by fitting the predictions to the experimental data. We obtain a correlation coefficient of 0.9915 for the following equation:

$$V_\varepsilon = 4.78 - 0.01T + 0.22H + 4.81 \times 10^{-6}T^2 - 0.24H^2 - 6.89 \times 10^{-5}TH. \tag{4}$$

The comparison of the predicted and experimental V_ε values obtained using Eq. (4) demonstrated an error rate within 20%, with a mean ratio value of 1.0154 and variance of 0.0841 (Fig. 14). This suggested that the fitted function could effectively predict V_ε for the concrete specimens after high-temperature exposure.

Figure 14: Comparison of predicted and tested values of modulus of elasticity of concrete specimens

4 Statistical Constitutive Damage Model

4.1 Model Establishment

Based on Lemaitre's equivalent strain hypothesis [52], the constitutive damage relationship for concrete specimens under high-temperature conditions can be expressed as

$$\sigma = E_0(1 - D)\varepsilon, \tag{5}$$

$$D = D_T + D_S - D_T D_S, \tag{6}$$

where σ is the stress; ε is the strain; E_0 is the elasticity modulus of the concrete specimen before high-temperature exposure; D is the total damage to the specimen; D_T is the damage at a given high temperature T; D_S is the load damage; and $D_\mathrm{T}D_\mathrm{S}$ is the coupling phase. The high-temperature damage can be defined as [53]

$$D_T = 1 - \frac{E_T}{E_{25}}, \tag{7}$$

where E_{25} and E_T are the elasticity moduli of concrete specimens at room temperature and a given high temperature T, respectively. The elasticity modulus can be computed as [54]

$$E = \frac{\sigma_2 - \sigma_1}{\varepsilon_2 - \varepsilon_1} \tag{8}$$

where σ_1 and σ_2 (ε_1 and ε_2) are the 20% and 80% peak stress (peak strain) values, respectively.

When concrete specimens are subjected to loading, the strength of their microelements conforms to the Weibull probability distribution [55]. The loading damage, D_S, can be defined as the ratio of the number of damaged microelements, N_f, to the total number of microelements, N_f, and can be expressed as

$$D_S = \frac{N_f}{N_t} = 1 - exp\left[-\left(\frac{\varepsilon}{a}\right)^m\right] \tag{9}$$

where m and a are the Weibull distribution parameters. By combining Eqs. (6)–(9), the total damage of the concrete specimens after high-temperature exposure can be expressed as

$$D = 1 - \frac{E_T}{E_{25}} exp\left[-\left(\frac{\varepsilon}{a}\right)^m\right]. \tag{10}$$

Substituting Eq. (10) into Eq. (5) yields the constitutive damage relationship for the concrete specimens after high-temperature exposure as

$$\sigma = E_T \varepsilon\, exp\left[-\left(\frac{\varepsilon}{a}\right)^m\right]. \tag{11}$$

The parameters m and a in Eq. (11) can be determined from the stress-strain curve peaks. The peaks represent the following boundary conditions: $\sigma = \sigma_c$, $\varepsilon = \varepsilon_c$, and $d\sigma/d\varepsilon = 0$, where σ_c and ε_c are the peak stress and strain, respectively. By solving the simultaneous equations, we obtain

$$\frac{d\sigma}{d\varepsilon}\bigg|_{\varepsilon = \varepsilon_c} = E_T exp^{\left[-\left(\frac{\varepsilon}{a}\right)^m\right]}\left[1 - m\left(\frac{\varepsilon_c}{a}\right)^m\right] = 0, \tag{12}$$

$$\sigma_c = E_T \varepsilon_c\, exp\left[-\left(\frac{\varepsilon}{a}\right)^m\right]. \tag{13}$$

Combining Eqs. (12) and (13) yields m and a as

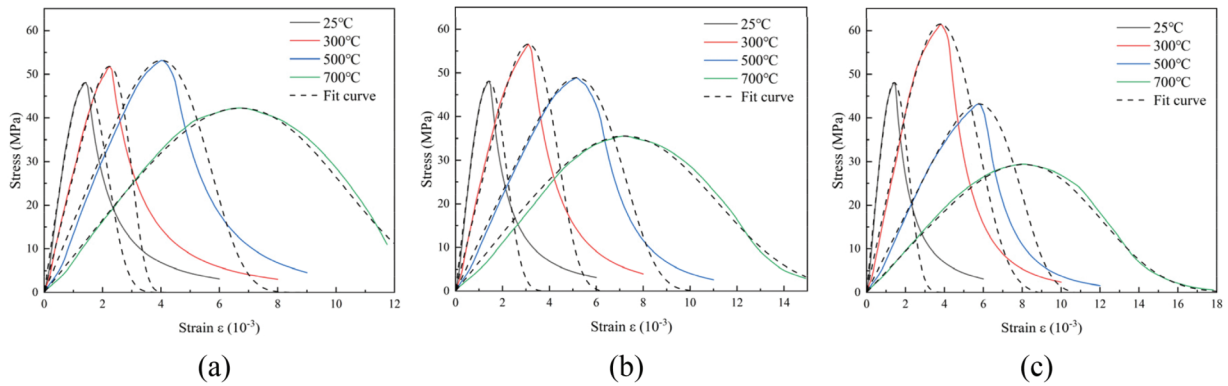$$m = \frac{1}{\ln\dfrac{E_T \varepsilon_c}{\sigma_c}}, \tag{14}$$

$$a = \frac{\varepsilon_c}{\left(\ln\dfrac{E_T \varepsilon_c}{\sigma_c}\right)^{\ln\frac{E_T \varepsilon_c}{\sigma_c}}}. \tag{15}$$

4.2 Damage Model Verification

By computing the stress-strain curves for the concrete specimens after exposure to different temperatures, the m and a values were obtained (Table 5). The values of these parameters reflect the influence of the different exposure temperatures on the degree of damage to the concrete specimens. By substituting these values in Eq. (11), we obtained the model-predicted stress-strain curves. The experimental stress-strain curves for the concrete specimens after high-temperature exposure demonstrated a good agreement with the constitutive model predictions (Fig. 15).
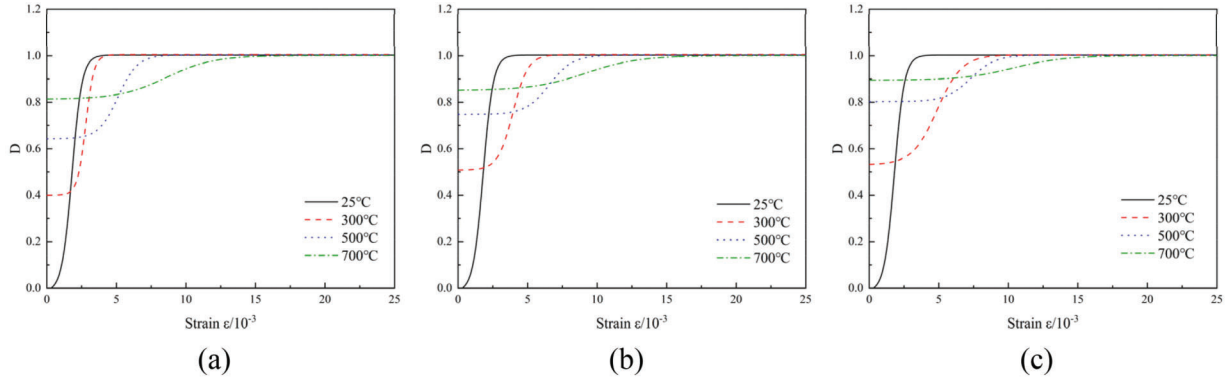
Table 5: Uniaxial constitutive damage model parameters

Number	E_0	σ_c	ε_c	m	a	R^2
T25	4521.378	48.1	0.014	3.456	0.020	0.9956
T300-H1	2694.675	51.8	0.022	6.615	0.030	0.9887
T300-H1.5	2218.817	55.6	0.031	5.106	0.043	0.9842
T300-H2	2097.953	61.4	0.038	3.809	0.054	0.9719
T500-H1	1612.297	53.2	0.040	5.079	0.055	0.9890
T500-H1.5	1137.441	48.9	0.052	5.439	0.071	0.9887
T500-H2	892.250	43.2	0.058	5.773	0.078	0.9444
T700-H1	834.600	42.3	0.067	3.536	0.096	0.9992
T700-H1.5	664.843	35.5	0.072	3.338	0.103	0.9966
T700-H2	472.475	29.4	0.081	3.861	0.114	0.9995

(a) (b) (c)

Figure 15: Experimental *vs.* predicted stress-strain curves for concrete specimens after high-temperature exposure for (a) 1.0, (b) 1.5, and (c) 2.0 h

4.3 Total Damage Evolution Characteristics

This study established a high-temperature damage model based on the Weibull distribution, which introduced load (D_S) and high-temperature (D_T) damage to intuitively reflect the initial damage to the concrete specimens due to high temperatures. With increasing strain, the total damage (D) to the concrete exhibited an exponential trend, approaching a value of 1 (Fig. 16). This phenomenon indicated that the concrete specimens experienced an evolutionary process from initial damage at high temperatures to gradual damage under compressive loads. For a thermostatic duration of 1 h, the initial degree of damage increased from 0.401 to 0.815 as the exposure temperature increased from 300°C to 700°C, suggesting significant damage to the concrete specimens. SEM analysis further indicated that (i) water evaporation within the specimens due to high temperatures; (ii) gradual decomposition of gelatinous materials, and (iii) inconsistent thermal expansion coefficients between the MSWI-BA aggregate and cement paste, resulted in the gradual expansion of internal cracks and increased initial damage. For a given exposure temperature, the initial degree of damage to the concrete specimens also increased with the increasing thermostatic durations. For example, at 500°C, as the thermostatic durations were increased from 1 to 2 h, the initial degree of damage increased from 0.643 to 0.803. This indicated that longer thermostatic durations enhanced the severity of the damage caused by high temperatures to the concrete specimens.

Figure 16: Relationship of total specimen damage, D, with the applied strain, ε, after high-temperature exposure for (a) 1.0, (b) 1.5, and (c) 2.0 h

5 Conclusion

In this study, we prepared concrete specimens with a 1% SF volume fraction and a 20% MSWI-BA fine aggregate replacement rate, and analyzed their performance at high temperatures (300°C–700°C) compared to room temperature for different thermostatic durations (1–2 h) using an electric resistance furnace. We further conducted uniaxial compression tests after high-temperature treatment. Based on our observations and analysis of the test results, the following conclusions were drawn:

- Below 500°C, the concrete surfaces do not show any obvious cracks; the microscopic matrix remains compact; and the macroscopic compressive strength increases. Above 500°C, the surfaces exhibited a significant number of cracks, with brownish-red traces of SFs oxidized due to the high temperature. The microscopic matrix becomes dispersed and its bonds with the SFs deteriorate, substantially decreasing the macroscopic compressive strength of the specimens.
- The mass loss rate of the concrete specimens gradually increases with the increasing exposure temperature and thermostatic duration. Below 500°C, it depends on the internal free water evaporation; above 500°C, it depends on the decomposition and loss of internal structure.
- With the increase of the exposure temperature and thermostatic duration, the stress-strain curve of the concrete specimens gradually smoothen. The compressive strength demonstrates a general trend of an initial increase and a subsequent decrease, with a rapid increase in peak strain and a decrease in elastic modulus.
- For different thermostatic durations, the critical temperature for the concrete specimens varies (700°C for 1.0 and 1.5 h, and 500°C for 2 h).
- Combining the strain equivalence hypothesis and Weibull distribution theory, a fitting model and total damage expression considering the coupling effect of temperature and compressive load were proposed, which can accurately reflect the influence of high temperatures on the macroscopic mechanical properties of MSWI-BA-and SF-reinforced concrete specimens.

Overall, our research results provide technical support for the performance evaluation of MSWI-BA-and SF-reinforced concrete after high-temperature exposure, aiding its potential application in engineering practice and the development of new green concrete fields. It is worth noting that the current research is limited to the effects of temperature and thermostatic durations, which is not enough to systematically understand the mechanical behavior of the composite concrete under high temperatures. Future works must focus on the influence of fiber content, fiber type, and MSWI-BA replacement rate on the tensile, bending, and compressive properties of the composite concrete over a wider temperature range.

References

1. Bawab, J., Khatib, J., Kenai, S., Sonebi, M. (2021). A review on cementitious materials including municipal solid waste incineration bottom ash (MSWI-BA) as aggregates. *Buildings, 11(5),* 19. https://doi.org/10.3390/buildings11050179

2. Li, J. Q. (2021). Municipal solid waste incineration ash-incorporated concrete: One step towards environmental justice. *Buildings, 11(11),* 24. https://doi.org/10.3390/buildings11110495

3. Loginova, E., Volkov, D. S., de Wouw, P., Florea, M. V. A., Brouwers, H. J. H. (2019). Detailed characterization of particle size fractions of municipal solid waste incineration bottom ash. *Journal of Cleaner Production, 207,* 866–874. https://doi.org/10.1016/j.jclepro.2018.10.022

4. Magnuson, J. K., Weiksnar, K. D., Patel, A. D., Clavier, K. A., Ferraro, C. C. et al. (2023). Processing municipal solid waste incineration bottom ash for integration into cement product manufacture. *Resources Conservation and Recycling, 198,* 11. https://doi.org/10.1016/j.resconrec.2023.107139

5. Zeng, C., Lyu, Y., Wang, D. H., Ju, Y. Z., Shang, X. Y. et al. (2020). Application of fly ash and slag generated by incineration of municipal solid waste in concrete. *Advances in Materials Science and Engineering, 2020,* 7802103. https://doi.org/10.1155/2020/7802103

6. Cheng, Y. Z., Dong, Y., Diao, J. K., Zhang, G. Y., Chen, C. et al. (2019). MSWI bottom ash application to resist sulfate attack on concrete. *Applied Sciences, 9(23),* 5091. https://doi.org/10.3390/app9235091

7. Loginova, E., Schollbach, K., Proskurnin, M., Brouwers, H. J. H. (2023). Mechanical performance and microstructural properties of cement mortars containing MSWI BA as a minor additional constituent. *Case Studies in Construction Materials, 18,* 16. https://doi.org/10.1016/j.cscm.2022.e01701

8. Mathews, G., Sinnan, R., Young, M. (2019). Evaluation of reclaimed municipal solid waste incinerator sands in concrete. *Journal of Cleaner Production, 229,* 838–849. https://doi.org/10.1016/j.jclepro.2019.04.387

9. Grazulyte, J., Vaitkus, A., Sernas, O., Zalimiene, L. (2022). The impact of MSWI bottom ash as aggregate on concrete mechanical performance. *International Journal of Pavement Engineering, 23(9),* 2903–2911. https://doi.org/10.1080/10298436.2021.1873333

10. Shang, M. G., Zhang, Y. S., He, Z. M., Qiao, H. X., Liu, X. Y. et al. (2023). Workability properties of specified density concrete with municipal solid waste incinerator tailings added as a lightweight aggregate. *Journal of Construction Engineering and Management, 149(8),* 17. https://doi.org/10.1061/JCEMD4.COENG-13148

11. Mathews, G., Dalesandro, K., Young, M., Soliman, M. (2021). Waste-to-energy reclaimed sands as lightweight aggregates for internally cured self-consolidated precast concrete. *Construction and Building Materials, 280,* 122545. https://doi.org/10.1016/j.conbuildmat.2021.122545

12. Liu, J., Niu, R., Hu, J., Ren, Y., Zhang, W. et al. (2023). The performance and microstructure of alkali-activated artificial aggregates prepared from municipal solid waste incineration bottom ash. *Construction & Building Materials, 403,* 133012.

13. Wang, Q., Chu, H. Y., Shi, W. F., Jiang, J. Y., Wang, F. J. (2023). Feasibility of preparing self-compacting mortar via municipal solid waste incineration bottom ash: An experimental study. *Archives of Civil and Mechanical Engineering, 23(4),* 16. https://doi.org/10.1007/s43452-023-00794-5

14. Li, H. R., Chu, H. Y., Wang, Q., Tang, J. H. (2023). Feasibility of producing eco-friendly self-compacting mortar with municipal solid waste incineration bottom ash: A preliminary study. *Case Studies in Construction Materials, 19,* 17. https://doi.org/10.1016/j.cscm.2023.e02309

15. Alderete, N. M., Joseph, A. M., van den Heede, P., Matthys, S., de Belie, N. (2021). Effective and sustainable use of municipal solid waste incineration bottom ash in concrete regarding strength and durability. *Resources Conservation and Recycling, 167,* 16. https://doi.org/10.1016/j.resconrec.2020.105356

16. Yao, J. W., Song, H., Li, Y. C., Cui, Y. Q., Chai, M. J. et al. (2023). Mechanism of macro-and microscopic performance of cement mortars influenced by municipal solid waste incineration bottom ash as sand substitution. *Construction and Building Materials, 397,* 10. https://doi.org/10.1016/j.conbuildmat.2023.132317

17. Liu, F., Liu, J., Wang, B. M., Yuan, X. S. (2023). Analysis of mechanical properties and pore structure of mortar prepared from municipal solid waste incineration slag. *Journal of Testing and Evaluation, 22,* 2780–2800. https://doi.org/10.1520/JTE20220650

18. Thomas, M., Slosarczyk, A. (2023). Effect of municipal solid waste slag on the durability of cementitious composites in terms of resistance to freeze-thaw cycling. *Materials, 16(2),* 20. https://doi.org/10.3390/ma16020626

19. Abubakr, A., Soliman, A. (2023). Impact behaviour of steel-fibre-reinforced alkali-activated slag concrete exposed to elevated temperatures. *Materials, 16(11),* 22. https://doi.org/10.3390/ma16114096

20. Colombo, M., di Prisco, M., Felicetti, R. (2010). Mechanical properties of steel fibre reinforced concrete exposed at high temperatures. *Materials and Structures, 43(4),* 475–491. https://doi.org/10.1617/s11527-009-9504-0

21. Kumari, G. J., Mousavi, S. S., Bhojaraju, C. (2023). Influence of thermal cycles and high-temperature exposures on the residual strength of hybrid steel/glass fiber-reinforced self-consolidating concrete. *Structures, 55,* 1532–1541. https://doi.org/10.1016/j.istruc.2023.06.096

22. Thamilpriya, V., Elangovan, G. (2023). Influence of quartz in self-compaction concrete at elevated temperature. *Journal of Ceramic Processing Research, 24(3),* 554–559. https://doi.org/10.36410/jcpr.2023.24.3.554

23. Xie, J. H., Zhang, Z., Lu, Z. Y., Sun, M. W. (2018). Coupling effects of silica fume and steel-fiber on the compressive behaviour of recycled aggregate concrete after exposure to elevated temperature. *Construction and Building Materials, 184,* 752–764. https://doi.org/10.1016/j.conbuildmat.2018.07.035

24. Li, X. G., Liu, Z. L., Lv, Y., Cai, L. X., Jiang, D. B. et al. (2018). Utilization of municipal solid waste incineration bottom ash in autoclaved aerated concrete. *Construction and Building Materials, 178,* 175–182. https://doi.org/10.1016/j.conbuildmat.2018.05.147

25. Zhang, B. B., Ma, Y., Yang, Y., Zheng, D. D., Wang, Y. et al. (2023). Improving the high temperature resistance of alkali-activated slag paste using municipal solid waste incineration bottom ash. *Journal of Building Engineering, 72,* 18. https://doi.org/10.1016/j.jobe.2023.106664

26. Zhang, P., Kang, L. Y., Wang, J., Guo, J. J., Hu, S. W. et al. (2020). Mechanical properties and explosive spalling behavior of steel-fiber-reinforced concrete exposed to high temperature—A review. *Applied Sciences, 10(7),* 2324. https://doi.org/10.3390/app10072324

27. Zhang, X. Y., Lin, X., Chen, Y. (2021). Study on mechanical properties of steel fiber reinforced nano-concrete (SFRNC) after elevated temperature. *Composite Structures, 268,* 19. https://doi.org/10.1016/j.compstruct.2021.113941

28. Zhuang, J. P., Xu, K., Chen, J. X., Wu, M. H. (2023). Dynamic stress-strain relationship of steel fiber-reinforced rubber self-compacting concrete after exposure to high temperature. *Structures, 57,* 105118. https://doi.org/10.1016/j.istruc.2023.105118

29. Guler, S., Akbulut, Z. F. (2022). Residual strength and toughness properties of 3D, 4D and 5D steel fiber-reinforced concrete exposed to high temperatures. *Construction and Building Materials, 327,* 10. https://doi.org/10.1016/j.conbuildmat.2022.126945

30. Lyu, X., Elchalakani, M., Ahmed, T., Sadakkathulla, M. A., Youssf, O. (2023). Residual strength of steel fibre reinforced rubberised UHPC under elevated temperatures. *Journal of Building Engineering, 76,* 20. https://doi.org/10.1016/j.jobe.2023.107173

31. Tang, C. W. (2019). Residual properties of high-strength fiber reinforced concrete after exposure to high temperatures. *Computers and Concrete, 24(1),* 63–71. https://doi.org/10.12989/cac.2019.24.1.063

32. Wang, H. L., Wei, M., Wu, Y. H., Huang, J. L., Chen, H. H. et al. (2021). Mechanical behavior of steel fiber-reinforced lightweight concrete exposed to high temperatures. *Applied Sciences, 11(1),* 116. https://doi.org/10.3390/app11010116

33. Alimrani, N. S., Balazs, G. L. (2021). Effect of steel fibres on concrete at different temperatures in terms of shear failure. *Magazine of Concrete Research, 73(21),* 1113–1124. https://doi.org/10.1680/jmacr.19.00479

34. Chen, G. M., He, Y. H., Yang, H., Chen, J. F., Guo, Y. C. (2014). Compressive behavior of steel fiber reinforced recycled aggregate concrete after exposure to elevated temperatures. *Construction and Building Materials, 71,* 1–15. https://doi.org/10.1016/j.conbuildmat.2014.08.012

35. Ding, Y. N., Azevedo, C., Aguiar, J. B., Jalali, S. (2012). Study on residual behaviour and flexural toughness of fibre cocktail reinforced self compacting high performance concrete after exposure to high temperature. *Construction and Building Materials, 26(1),* 21–31. https://doi.org/10.1016/j.conbuildmat.2011.04.058

36. Yang, L., Lü, J., Xie, H., Yang, D., Fan, P. et al. (2023). Experimental study on uniaxial compressive properties and damage evolution of basalt fiber reinforced concrete after being subjected to high temperature. *Structures, 54,* 693–703. https://doi.org/10.1016/j.istruc.2023.05.089

37. Shen, L., di Luzio, G., Cao, M. S., Ren, Q. W., Ren, X. H. et al. (2023). Insights and theoretical model of thermal conductivity of thermally damaged hybrid steel-fine polypropylene fiber-reinforced concrete. *Cement & Concrete Composites, 138,* 16. https://doi.org/10.1016/j.cemconcomp.2023.105001

38. Shen, L., Yao, X. P., Zhu, D., Alkayem, N. F., Cao, M. S. et al. (2021). A thermal cracking pattern-based multiscale homogenization method for effective thermal conductivity of steel fiber reinforced concrete after high temperature. *International Journal of Heat and Mass Transfer, 180,* 11. https://doi.org/10.1016/j.ijheatmasstransfer.2021.121732

39. Yu, X., Chen, L., Fang, Q., Ruan, Z., Hong, J. et al. (2017). A concrete constitutive model considering coupled effects of high temperature and high strain rate. *International Journal of Impact Engineering, 101,* 66–77. https://doi.org/10.1016/j.ijimpeng.2016.11.009

40. Gebuhr, G., Pise, M., Sarhil, M., Anders, S., Brands, D. et al. (2019). Analysis and evaluation of the pull-out behavior of hooked steel fibers embedded in high and ultra-high performance concrete for calibration of numerical models. *Structural Concrete, 20(4),* 1254–1264. https://doi.org/10.1002/suco.201900034

41. Singh, D., Kumar, A. (2023). Performance studies of fiber-reinforced municipal solid waste incineration bottom ash amended with cement for Geotechnical applications. *Sadhana-Academy Proceedings in Engineering Sciences, 48(3),* 117. https://doi.org/10.1007/s12046-023-02171-7

42. Ju, Y., Liu, H. B., Liu, J. H., Tian, K. P., Wei, S. et al. (2011). Investigation on thermophysical properties of reactive powder concrete. *Science China-Technological Sciences, 54(12),* 3382–3403. https://doi.org/10.1007/s11431-011-4536-4

43. Li, Z. H., Li, B., Zhang, F. (2021). Mechanical properties of fiber nano-modified rubber concrete in high temperature. *Ferroelectrics, 580(1),* 71–84. https://doi.org/10.1080/00150193.2021.1905726

44. Shen, D. J., Liu, X. Z., Li, Q. Y., Sun, L., Wang, W. T. (2019). Early-age behavior and cracking resistance of high-strength concrete reinforced with Dramix 3D steel fiber. *Construction and Building Materials, 196,* 307–316. https://doi.org/10.1016/j.conbuildmat.2018.10.125

45. Cui, K., Xu, L., Li, L., Chi, Y. (2023). Mechanical performance of steel-polypropylene hybrid fiber reinforced concrete subject to uniaxial constant-amplitude cyclic compression: Fatigue behavior and unified fatigue equation. *Composite Structures, 311,* 116795.

46. Li, S., Zheng, W., Zhou, W., Jiang, Z., Cui, Y. (2023). Local compression capacity of steel fiber reinforced ultra-high performance concrete containing coarse aggregate. *Composite Structures, 318,* 117084.

47. Varona, F. B., Baeza, F. J., Bru, D., Ivorra, S. (2018). Evolution of the bond strength between reinforcing steel and fibre reinforced concrete after high temperature exposure. *Construction and Building Materials, 176,* 359–370. https://doi.org/10.1016/j.conbuildmat.2018.05.065

48. Zhang, H. Y., Qiu, G. H., Kodur, V., Yuan, Z. S. (2020). Spalling behavior of metakaolin-fly ash based geopolymer concrete under elevated temperature exposure. *Cement & Concrete Composites, 106,* 13. https://doi.org/10.1016/j.cemconcomp.2019.103483

49. Li, L., Zhang, R. B., Jin, L., Du, X. L., Wu, J. et al. (2019). Experimental study on dynamic compressive behavior of steel fiber reinforced concrete at elevated temperatures. *Construction and Building Materials, 210,* 673–684. https://doi.org/10.1016/j.conbuildmat.2019.03.138

50. Abdallah, S., Fan, M. Z., Cashell, K. A. (2017). Bond-slip behaviour of steel fibres in concrete after exposure to elevated temperatures. *Construction and Building Materials, 140,* 542–551. https://doi.org/10.1016/j.conbuildmat.2017.02.148

51. Yao, Y., Fang, H., Guo, H. C. (2022). Unified damage constitutive model for fiber-reinforced concrete at high temperature. *Journal of Engineering Mechanics, 148(1).* https://doi.org/10.1061/(ASCE)EM.1943-7889.0002057

52. Lemaitre, J., Chaboche, J. L. (1990). *Mechanics of solid materials: Contents.* Cambridge University Press.

53. Xie, J., Li, X., Wu, H. (2014). Experimental study on the axial-compression performance of concrete at cryogenic temperatures. *Construction & Building Materials, 72,* 380–388. https://doi.org/10.1016/j.conbuildmat.2014.09.033

54. Maekawa, K., Pimanmas, A., Okamura, H. (2003). *Nonlinear mechanics of reinforced concrete.* Spon Press.

55. Cao, W., Zhao, M., Liu, C. (2004). Study on the model and its modifying method for rock softening and damage based on weibull random distribution. *Chinese Journal of Rock Mechanics and Engineering, 23(19),* 3226–3231. https://doi.org/10.3321/j.issn:1000-6915.2004.19.003